

Optimizing the Optical Properties of Tin Oxide Aerogels through Defect Passivation

John F. Hardy II^{a,b,*}, Madison King^{a,c}, Stephanie Hurst^{a,c}, Carlo R. daCunha^{a,b}

^a*Center for Materials Interfaces in Research and Applications, Northern Arizona University, 700 Osborn Dr., Flagstaff, 86011, AZ, USA*

^b*School of Informatics, Computer, and Cyber Systems, Northern Arizona University, 1295 Knoles Drive, Flagstaff, 86011, AZ, USA*

^c*Department of Chemistry and Biochemistry, Northern Arizona University, 700 Osborn Dr., Flagstaff, 86011, AZ, USA*

Abstract

Tin oxide aerogels were synthesized using an epoxide-assisted technique and characterized with Fourier transform infrared, X-ray diffraction, and UV-Vis to study the effects of post-synthesis annealing and peroxide treatment. While bulk tin oxide exhibits an optical bandgap of 3.6 eV, its aerogel form often displays a larger apparent bandgap around 4.6 eV due to defects. Our study reveals that annealing induces a partial phase change from SnO₂ to SnO, but is ineffective in removing defects. Conversely, peroxide passivation effectively lowers the bandgap and disorder levels, suggesting that dangling bonds are the primary cause of the increased bandgap in tin oxide aerogels. These findings offer insights for optimizing the optical properties of tin oxide aerogels for applications like solar cells.

Keywords: Aerogel, Annealing, Passivation, Semiconducting, SnO₂

1. Introduction

Tin oxide (SnO₂) has received attention in recent years due various applications, such as gas sensing [1], catalysis [2], and energy storage [3, 4]. This is a wide bandgap, unintentionally doped n-type semiconductor that is known for its high optical transparency and low electrical resistance [5]. The possibility of fabricating SnO₂ aerogels further increases its applicability in space applications [6] and as a thermal insulator [7] because of high surface areas, low

*Corresponding author. Email: jfh67@nau.edu

density, and tunable electrical conductivity [8, 9]. However, the performance of SnO₂ aerogels in these applications is often limited by surface defects, which can significantly alter their electronic structure and optical properties [10].

In this study, we investigate the impact of surface defects on the electronic properties of SnO₂ aerogels, with a particular focus on their influence on the bandgap. Our research reveals that the presence of surface defects leads to an apparent increase in the bandgap, potentially affecting the material's performance. Bulk SnO₂ exhibits an optical bandgap energy (E_g) of 3.6 eV, while SnO₂ in aerogel form shows an apparent E_g around 4.6 eV, which significantly limits its electrical conductivity due to the reduced number of available charge carriers [11, 12, 13]. Surface defects, particularly dangling bonds on Sn-rich surfaces, lead to a Burstein-Moss shift [14, 15, 16]. This phenomenon elevates the Fermi level, resulting in both an apparent increase in the bandgap (E_g) and the formation of additional surface states, which significantly affect the material's electronic behavior [17, 18, 19]. To address this issue, we explore different strategies for defect passivation, aiming to optimize the electronic properties of SnO₂ aerogels while maintaining its unique structural characteristics.

Initially, we examined a conventional annealing approach as a means to passivate surface defects [20, 21]. However, our findings demonstrate that this method, while traditionally effective in reducing defects, ultimately compromises its structure [13]. On the other hand, we demonstrate that aging the hydrogel phase in hydrogen peroxide (H₂O₂) results in a significant reduction of the apparent bandgap. Crucially, this strategy maintains the structural integrity of the material, overcoming the limitations observed with traditional annealing techniques.

Our work provides new insights into the nature of surface defects in high-surface area SnO₂ aerogels and offers a promising route for their mitigation.

The findings presented here have the potential to enhance the performance of SnO₂ aerogels in various applications, paving the way for their improved use in next-generation devices and technologies.

The structure of this paper is the following. Next, we discuss the materials and methods used to fabricate and measure the material. We then present the results obtained using Fourier transform infrared spectroscopy (FTIR), Williamson-Hall (WH) analysis performed on X-ray diffraction data (XRD), and ultraviolet-visible spectroscopy (UV-Vis).

2. Materials and Methods

All the chemicals used in the synthesis process were purchased from Sigma Aldrich and were used as received without further purification. An epoxide method was used to synthesize the SnO₂ aerogels [22]. In a typical synthesis, 0.65 g of tin tetrachloride pentahydrate (SnCl₄·5H₂O) was dissolved in a 1:2 co-solvent mixture of ethanol (EtOH) and water (H₂O) under magnetic stirring for 2 minutes. After the complete dissolution of the tin precursor, 0.8 ml of propylene oxide (CH₃CHCH₂O) was gradually added to the solution. The mixture was immediately poured into a silicone mold, initiating hydrogel formation within 40 seconds. The hydrogel was aged in 200-proof ethanol for 24 hours, followed by a solvent exchange. Subsequently, a critical point drying process using liquid CO₂ was employed to convert the hydrogel into an aerogel using a Pelco CPD-2 critical point dryer. Figure 1 shows a high-resolution transmission electron microscope (HRTEM) image of the formed aerogel using a Talos F200i TEM.

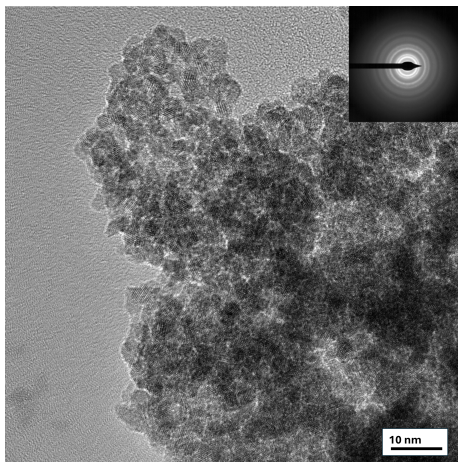


Fig. 1: HRTEM image of the nanocrystallite array of the unannealed aerogel structure. A collection of nanocrystallites with an average diameter of 2.53 nm is visible in the image.

From the HRTEM image of the unannealed aerogel, the average crystallite size was calculated to be 2.53 nm, and the rings in the selected area electron diffraction (SAED) pattern reveal that the SnO_2 aerogel is polycrystalline. By measuring the radius of the rings, the interplanar spacing can be calculated as [23, 24]:

$$d_{hkl} = \frac{L\lambda}{R}, \quad (1)$$

where d_{hkl} is the interplanar spacing of the crystal planes with Miller indices (hkl) , L is the distance from the specimen to the detector, λ is the electron wavelength, and R is the radius of the diffraction ring. SnO_2 has a tetragonal crystal rutile structure, and the hkl indices are calculated as [25]:

$$\frac{1}{d_{hkl}^2} = \frac{h^2 + k^2}{a^2} + \frac{l^2}{c^2}, \quad (2)$$

where $a = 4.836\text{\AA}$ and $c = 3.2742\text{\AA}$ are the lattice parameters of the tetragonal structure [26]. From the diffraction pattern of the HRTEM image, the crystal planes most prominent are (110), (101), (211), (112), (212), and (322).

Once the aerogel was formed, the material underwent annealing at atmospheric pressure in a tube furnace at temperatures of 100°C, 200°C, 300°C, and 400°C for 30 minutes each to study the effects of annealing on the crystalline structure of the SnO₂ aerogels. During the annealing procedure, the samples were exposed to the oxygen from the environment to passivate possible dangling bonds. Additionally, to passivate the dangling bonds on the material’s surface without annealing, a tin oxide hydrogel sample was aged for 24 hours in a 3% H₂O₂:H₂O solution.

FTIR (Bruker Alpha Spectrometer) was utilized to analyze the chemical composition of the aerogel and identify any potential contaminants or unreacted precursors. Each sample was fragmented into smaller pieces for analysis.

A Rigaku Miniflex 6G with an ASC-8 powder sample attachment was used to perform XRD measurements on the powdered samples. The peaks in the diffractograms obtained from each sample were fitted with Gaussian curves to obtain peak broadenings. To calculate the crystallite size, the Debye-Scherrer equation was used [27]:

$$D = \frac{K\lambda}{B_{hkl}\cos(\theta)}. \quad (3)$$

In this equation, D is the crystallite size and K is Sherrer’s constant. We assumed $K = 0.94$ for spherical crystallites with cubic symmetry [28]. $\lambda = 1.54056 \text{ \AA}$ is the incident wavelength, B_{hkl} is the full-width at half maximum (FWHM) of the peaks, and θ is the peak position for the corresponding hkl plane. With Eq. 3, the Williamson-Hall method was implemented to find the strain of the crystallites. This was performed using the Williamson-Hall equation [29]:

$$\beta\cos(\theta) = C\epsilon\sin(\theta) + \frac{K\lambda}{D}. \quad (4)$$

We used $C = 4$ as a constant related to the train and strain distribution [30, 31].

Also in the equation ϵ is the strain, K is Scherrer's constant, λ is the incident wavelength, and D is the crystallite size. The strain was calculated with the slope of a linear regression of $\sin(\theta)$ as a function of $\beta \cdot \cos(\theta)$ for each sample.

UV-Vis was performed using an Agilent Cary 60 UV-Vis spectrophotometer. A reference of ethanol in a cuvette was taken, and then powdered aerogel was added to the ethanol for measurement to find the E_g and the Urbach energy (E_u) [32]. The Urbach energy represents the width of the tail of localized states in the bandgap, extending from the band edges into the forbidden gap. A larger Urbach energy indicates a higher degree of disorder in the material. This disorder can be due to various factors such as impurities or structural defects. The Urbach energy was obtained from the tail equation [33]:

$$\alpha = \alpha_0 \exp\left(\frac{h\nu - E_g}{E_u}\right), \quad (5)$$

where α_0 is the absorption constant, h is Planck's constant, ν is the photon wavelength, E_g is the optical bandgap energy, and E_u is the Urbach energy. By taking the natural logarithm of the absorption coefficient and plotting this data against photon energy ($h\nu$), a linear fit was applied to the absorption data in the Urbach tail region. The E_u was then derived from the inverse of the slope.

In optical experiments, Beer-Lambert's law was used to calculate the absorbance expressed by the equation [34]:

$$\alpha = \log_{10}\left(\frac{I_o}{I}\right), \quad (6)$$

where I_o is the incident light, I is the transmitted light to the spectrophotometer, and α is the absorbance. The absorbance α was later used in Tauc's

equation to calculate E_g [35]:

$$(\alpha h\nu)^{1/\gamma} = \alpha_0(h\nu - E_g), \quad (7)$$

where h is the Plank's constant, ν is the photon's frequency, and γ is the factor determined by the nature of the electronic transition involved. In the study of SnO₂ aerogels, $1/\gamma$ is assumed to be 2 corresponding to a direct transition, and α_0 is the energy-independent constant [36].

3. Results

The FTIR spectrum of the samples in Fig. 2 reveals distinct peaks corresponding to C-H stretching at 2990–3000 cm^{-1} , C-O stretching at 1040–1050 cm^{-1} and 1130–1140 cm^{-1} . The large feature at 530 cm^{-1} can be attributed to Sn-O stretching [13].

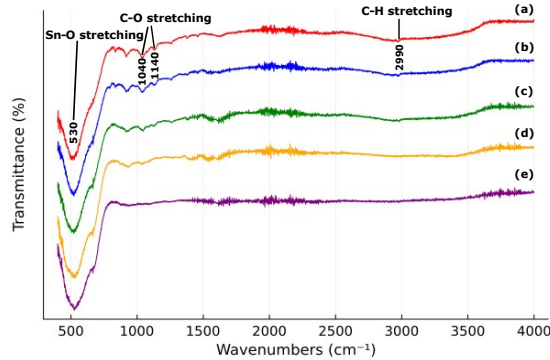


Fig. 2: FTIR spectrum of the unannealed sample (a) and the annealed samples at 100°C (b), 200°C (c), 300°C (d), and 400°C (e).

The obtained C-O and C-H stretching bands can be attributed to residual impurities containing carbon and hydroxyl groups. The influence of annealing on impurities is illustrated in Figure 3, which depicts the transmittance corresponding to impurity peaks at varying temperatures.

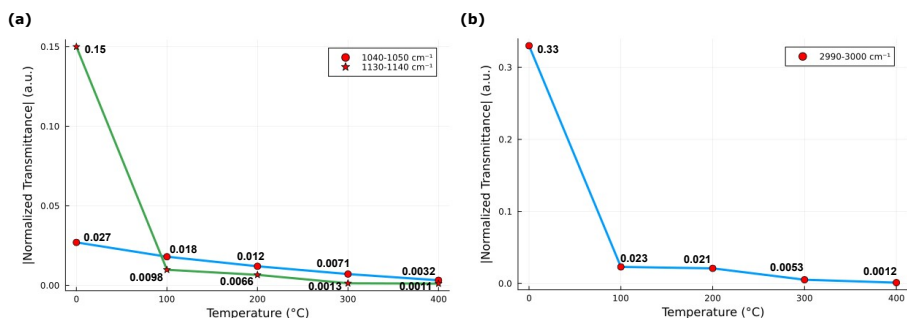


Fig. 3: Transmission intensities corresponding to: a) C-O stretching, and b) C-H stretching.

The graphs were normalized to a baseline of zero to visualize the relative changes in transmittance. Each data point represents the magnitude of transmittance of each peak height, and the reduction in transmittance suggests that fewer impurities are present at higher temperature. Figure 3 demonstrates a trend in both C-O and C-H stretching which indicates that impurities are reduced as the annealing process progresses.

The XRD results for the Debye-Scherrer equation, Eq. 3, for each temperature is illustrated in Fig. 4(a). Through this method, the average crystallite sizes are calculated at each temperature. The average crystallite size of the unannealed sample, measured using XRD, was found to be 2.5 nm, which is in close agreement with the value of 2.53 nm obtained from electron diffraction.

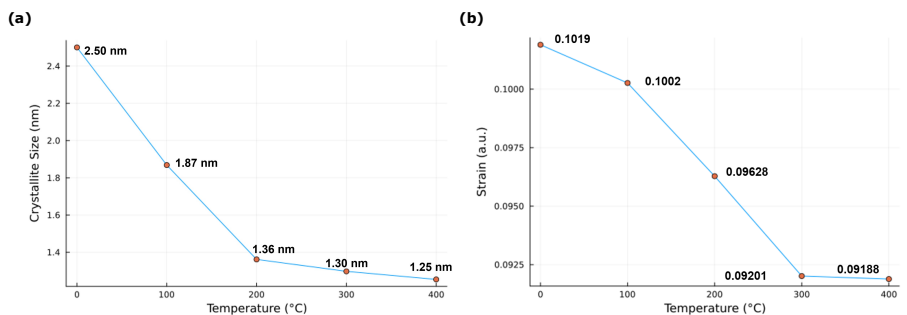


Fig. 4: a) Crystallite sizes calculated with Debye-Scherrer equation, and b) the strain of the crystal calculated with the Williamson-Hall equation.

By applying the Debye-Scherrer equation, the Williamson-Hall method (Eq. 4) was implemented to analyze the strain of the crystallites. These results are shown in Fig. 4(b). The crystallite size exhibits a near linear decrease from room temperature to 200°, with a rate of shrinkage of approximately 6 pm/°C. Beyond 200°, the rate of shrinkage significantly diminishes, reaching approximately 0.55 pm/°C. Strain reduces approximately 5.5% from room temperature up to 300°.

The apparent bandgaps obtained from applying Eq. 7 on Tauc plots are shown in Fig. 5(a), while the corresponding Urbach energies are shown in Fig. 5(b). The bandgap decreases at a nearly linear rate of approximately -3.15 meV/° from room temperature to 400°. The Urbach energy has a four-fold increase between room temperature to 300° but then drops by 63 % at 400°. This drop at 300° is consistent with our measurements of strain and aligns with the expected phase transition from SnO₂ to SnO that begins at approximately 300° [37].

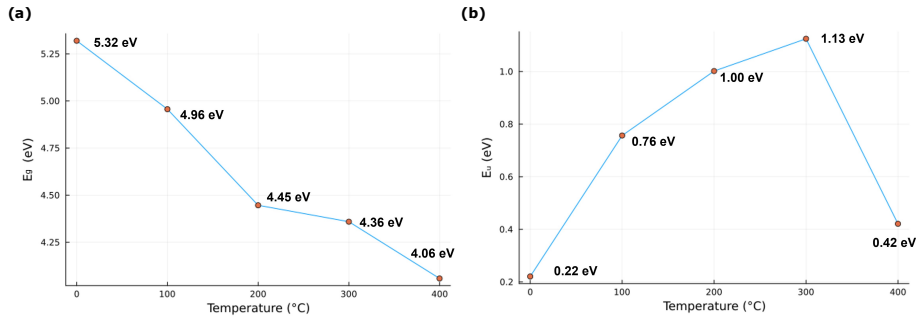


Fig. 5: a) Bandgap energies (E_g) as a function of the annealing temperature, and b) the corresponding Urbach energy (E_u).

The optical properties of the unannealed, peroxide-passivated samples are detailed in Table I.

	Control	H ₂ O ₂
E_u	0.2207 eV	0.147 eV
E_g	5.32 eV	3.64 eV

Table I: Urbach energy (E_u) and bandgap energy (E_g) for control unannealed and peroxide-passivated samples.

Since there were no annealing treatments performed on the peroxide-passivated sample, the XRD and FTIR results are comparable to the control unannealed sample.

4. Discussion

While annealing removes the impurities of the sample at each temperature as shown explicitly in Fig. 3, the positive effect of annealing is due to a partial phase change that occurs at around 300°C [37]. In the XRD peaks shown in Fig. 6, some peaks begin to broaden and disappear at 300°C. Around 400°C, a new peak begins to emerge at $2\theta = 37^\circ$ which corresponds to the (002) planes of SnO [38].

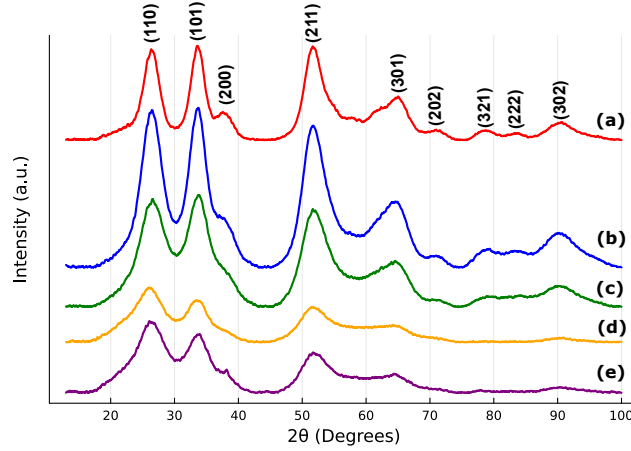


Fig. 6: XRD patterns of the a) unannealed sample and the annealed samples at b) 100°C, c) 200°C, d) 300°C (d), and e) 400°C.

This indicates there is a partial phase change from SnO₂ to SnO, and this

reduction is due to oxygen loss during annealing [39]. This behavior aligns with findings from previous literature where it was demonstrated that thermal activation of metal-oxide aerogels leads to the generation of oxygen vacancies [40]. We have previously shown through photoluminescence measurements that oxygen vacancies and oxygen complexes such as $(\text{Sn}_i^{+4} + \text{V}_0)^0$ are prevalent in sol-gel fabricated SnO₂ hydrogels [13]. These defects not only facilitate the phase change but also significantly influence the material's electronic properties by increasing the number of electron trapping sites. This partial phase change would explain why the crystallite size decreases in the results of the Debye-Scherrer equation shown in Fig. 4(a). It can be concluded that the oxygen loss causes the SnO₂ crystallites to become thermodynamically unstable, and they break down into smaller SnO crystallites that are more stable at the given annealing temperature. This partial phase change can also be seen in the E_u depicted in Fig. 5(b) as well. In the unannealed sample, the disorder is quantified by an Urbach energy of 0.22 eV which suggests that there are fewer localized states within the bandgap, and as more oxygen vacancies are created more localized states and disorder is seen within the material. At 300°C, the highest state of disorder is seen with the E_u reaching 1.13 eV. Once the material stabilizes at 400°C the E_u decreases to 0.42 eV, indicating a more ordered state, likely due to the phase change stabilizing the material. The formation of SnO is favored at higher temperatures, where the energy required for oxygen vacancy formation is compensated by the release of heat during the reduction. The cause for this partial phase change can be attributed to the negative enthalpy of the formation of SnO [41], indicating that the system achieves greater stability as it loses oxygen. Even with the creation of the oxygen vacancies and the partial phase change, Fig. 4(b) shows that as the SnO phase forms, the material enters a more stable, relaxed state and annealing further reduces strain by relieving structural defects

and grain boundary stresses. The reduction in the E_g can also be attributed to the partial phase change since SnO has a narrower E_g than SnO₂. Moreover, after the phase becomes more stable at 400°C, there is still an apparent E_g of 4.06 eV while SnO has a E_g typically within the range of 1.75–3.4 eV [42, 43]. When the unannealed sample is compared to the sample treated with H₂O₂, the E_u is reduced from 0.2207 eV to 0.147 eV (a 33 % improvement), and the E_g is also significantly reduced from 5.32 eV to 3.64 eV which is close to the expected E_g of SnO₂. This strongly supports the idea thesis the apparent E_g is heavily influenced by the dangling bonds on the surface of the material. H₂O₂ is a strong oxidizing agent, and when it interacts with reactive dangling bonds, the H₂O₂ donates oxygen to the surface, filling the dangling bonds and passivating the surface. Similar effects were demonstrated in studies of H₂O₂ on Ge(100), where the dangling bonds were significantly reduced compared to H₂O passivation [44].

5. Conclusions

In this study, SnO₂ aerogels were synthesized using an epoxide technique, and the effects of post-synthesis annealing and H₂O₂ passivation on surface defects were investigated to optimize the materials electronic properties for potential use in electronic applications. SnO₂ aerogel was shown to exhibit an increased apparent bandgap due to surface defects when compared to the typical bandgap of bulk SnO₂. Annealing the aerogels induces a partial phase change from SnO₂ to SnO, which creates oxygen vacancies, reduces strain in the material, and leads to a moderate improvement in the materials properties. This phase change does not fully address surface defects, but passivation with H₂O₂ effectively reduces both the bandgap and disorder in the material without compromising structural integrity, suggesting that surface dangling bonds sig-

nificantly contribute to the increased bandgap. In conclusion, while annealing has some benefits, H_2O_2 passivation offers a more efficient way to enhance the electronic properties of SnO_2 aerogels by minimizing surface defects and lowering the E_g . These findings provide new insights into the potential of SnO_2 aerogels for electronic applications such as solar cells and sensors.

6. Acknowledgements

The research was sponsored by the Army Research Laboratory and was accomplished under Cooperative Agreement Number W911NF-23-2-0014. The views and conclusions contained in this document are those of the authors and should not be interpreted as representing the official policies, either expressed or implied, of the Army Research Laboratory or the U.S. Government. The U.S. Government is authorized to reproduce and distribute reprints for Government purposes notwithstanding any copyright notation herein.

This material is also based upon work supported by the National Science Foundation under Grant No. 2425226.

7. Conflict of Interest

The authors declare that they have no conflict of interest.

References

- [1] P. Gupta and V. Rathore. A comprehensive review: SnO₂ for photovoltaic and gas sensor applications. *Appl. Innov. Res.*, 1:184–193, 2019.
- [2] P. Manjunathan and G. V. Shanbhag. 18 - application of tin oxide-based materials in catalysis. In M. O. Orlandi, editor, *Tin Oxide Materials*, Metal Oxides, pages 519–553. Elsevier, 2020.
- [3] S. R. Mishra and Md. Ahmaruzzaman. Tin oxide based nanostructured materials: synthesis and potential applications. *Nanoscale*, 14:1566–1605, 2022.
- [4] K. Kumari and Md. Ahmaruzzaman. SnO₂ quantum dots (qds): Synthesis and potential applications in energy storage and environmental remediation. *Mater. Res. Bull.*, 168:112446, 2023.
- [5] G. Kiruthiga, K. S. Rajni, N. Geethanjali, T. Raguram, E. Nandhakumar, and N. Senthilkumar. SnO₂: Investigation of optical, structural, and electrical properties of transparent conductive oxide thin films prepared by nebulized spray pyrolysis for photovoltaic applications. *Inorg. Chem. Commun.*, 145:109968, 2022.
- [6] L. W. Hrubesh. Aerogel applications. *J. Non. Cryst. Solids*, 225:335, 1998.
- [7] S. M. Jones. Aerogel: Space exploration applications. *J. Sol-Gel Sci. Technol.*, 40:351, 2006.
- [8] D. Mohanta and M. Ahmaruzzaman. Tin oxide nanostructured materials: an overview of recent developments in synthesis, modifications and potential applications. *RSC Adv.*, 6:110996–111015, 2016.
- [9] R.V. Morales, C.R. da Cunha, and C.R. Rambo. A complex network approach for the growth of aerogels. *Physica A*, 406:131–138, 2014.
- [10] S. O. Kucheyev, T. F. Baumann, P. A. Sterne, Y. M. Wang, T. van Buuren, A. V. Hamza, L. J. Terminello, and T. M. Willey. Surface electronic states in three-dimensional SnO₂ nanostructures. *Phys. Rev. B*, 72:035404, Jul 2005.
- [11] N. Haddad, Z. Ben Ayadi, H. Mahdhi, and K. Djessas. Influence of fluorine doping on the microstructure, optical and electrical properties of SnO₂ nanoparticles. *J. Mater. Sci. Mater. Electron.*, 28(20):15457–15465, 2017.
- [12] Vinayak B. Kamble and Arun M. Umarji. Defect induced optical bandgap narrowing in undoped SnO₂ nanocrystals. *AIP Adv.*, 3(8):082120, 08 2013.
- [13] C. R. da Cunha, G. H. Toffolo, C. E. I. dos Santos, and R. P. Pezzi. Structural, optical and chemical characterizations of sol-gel grown tin oxide aerogels. *J. Non. Cryst. Solids*, 380:48–52, 2013.

- [14] Z. M. Jarzebski and J. P. Marton. Physical properties of SnO₂ materials: I . preparation and defect structure. *J. Electrochem. Soc.*, 123(7):199C, 1976.
- [15] S. O. Kucheyev, T. F. Baumann, P. A. Sterne, Y. M. Wang, T. van Buuren, A. V. Hamza, L. J. Terminello, and T. M. Willey. Surface electronic states in three-dimensional SnO₂ nanostructures. *Phys. Rev. B*, 72:035404, Jul 2005.
- [16] S. Das and V. Jayaraman. SnO₂: A comprehensive review on structures and gas sensors. *Prog. Mater. Sci*, 66:112, 2014.
- [17] Z. Zhu, G. Ouyang, and G. Yang. Bandgap shift in SnO₂ nanostructures induced by lattice strain and coordination imperfection. *J. Appl. Phys.*, 108(8):083511, 2010.
- [18] W. Izydorczyk, B. Adamowicz, M. Miczek, and K. Waczynski. Computer analysis of an influence of oxygen vacancies on the electronic properties of the sno₂ surface and near-surface region. *Phys. Status Solidi A*, 203(9):2241–2246, 2006.
- [19] P. K. Chakraborty, G. C. Datta, and K. P. Ghatak. The simple analysis of the Burstein–Moss shift in degenerate n-type semiconductors. *Physica B Condens. Matter.*, 339:198, 2003.
- [20] M. Zarrinkhameh, A. Zendehnam, S. M. Hosseini, N. Robotmili, and M. Arabzadegan. Effect of oxidation and annealing temperature on optical and structural properties of sno₂. *Bull. Mater. Sci.*, 37(3):533–539, 2014.
- [21] P. V. Tuan, L. T. Hieu, C. M. Hoang, H. B. Tuong, V. T. Tan, T. T. Q. Hoa, N. X. Sang, and T. N. Khiem. Effects of annealing temperature on the structure, morphology, and photocatalytic properties of sno₂/rgo nanocomposites. *Nanotechnology*, 32(1):015201, 2020.
- [22] T. F. Baumann, S. O. Kucheyev, A. E. Gash, and J. H. Satcher Jr. Facile synthesis of a crystalline, high-surface-area SnO₂ aerogel. *Adv. Mater.*, 17:1546, 2005.
- [23] M. Janecek and R. Kral. *Modern Electron Microscopy in Physical and Life Sciences*. IntechOpen, 2016.
- [24] Henry Solomon Lipson. Elements of x-ray diffraction. *Contemporary Physics*, 20:87–88, 1979.
- [25] V.S. Jahnvi, S. K. Tripathy, and A. V. N. Ramalingeswara Rao. Structural, optical, magnetic and dielectric studies of sno₂ nano particles in real time applications. *Physica B: Condensed Matter*, 61:565, 2019.

- [26] Matthias Batzill, Khabibulakh Katsiev, James M. Burst, Ulrike Diebold, Anne M. Chaka, and Bernard Delley. Gas-phase-dependent properties of SnO₂ (110), (100), and (101) single-crystal surfaces: Structure, composition, and electronic properties. *Physical Review B*, 72(16):165414, October 2005.
- [27] S. Mustapha, M. M. Ndamitso, A. S. Abdulkareem, J. O. Tijani, D. T. Shuaib, A. K. Mohammed, and A. Sumaila. Comparative study of crystallite size using Williamson-Hall and Debye-Scherrer plots for ZnO nanoparticles. *Adv. Nat. Sci.: Nanosci. Nanotechnol.*, 10:045013, 2019.
- [28] J. I. Langford and A. J. C. Wilson. Scherrer after sixty years: A survey and some new results in the determination of crystallite size. *J. Appl. Crystallogr.*, 11:102, 1978.
- [29] D. Nath, F. Singh, and R. Das. X-ray diffraction analysis by Williamson-Hall, Halder-Wagner and size-strain plot methods of CdSe nanoparticles, a comparative study. *Mater. Chem. Phys.*, 239:122021, 2020.
- [30] A. R. Stokes and A. J. C. Wilson. The diffraction of X-rays by distorted crystal aggregates - I. *Proc. Phys. Soc.*, 56:174, 1944.
- [31] B. Himabindu, N. S. M. P. Latha Devi, and B. Rajini Kanth. Microstructural parameters from X-ray peak profile analysis by Williamson-Hall models; a review. *Mater. Today*, 47:4891, 2021.
- [32] Franz Urbach. The long-wavelength edge of photographic sensitivity and of the electronic absorption of solids. *Phys. Rev.*, 92:1324–1324, 1953.
- [33] P. Chetri and A. Choudhury. Investigation of optical properties of SnO₂ nanoparticles. *Physica E Low Dimens. Syst. Nanostruct.*, 47:257, 2013.
- [34] H. Zhao L. Li, Y. Wang N. Ni, J. Gao, Q. Gao, Y. Zhang, and Y. Zhang. Study on the origin of linear deviation with the Beer-Lambert law in absorption spectroscopy by measuring sulfur dioxide. *Spectrochim. Acta A Mol. Biomol. Spectrosc.*, 275:121192, 2022.
- [35] A. J. Deotale and R. V. Nandedkar. Correlation between particle size, strain and band gap of iron oxide nanoparticles. *Mater. Today*, 3:2069, 2016.
- [36] M.-M. Bagheri-Mohagheghi, N. Shahtahmasebi, M. R. Alinejad, A. Youssefi, and M. Shokooh-Saremi. The effect of the post-annealing temperature on the nano-structure and energy band gap of SnO₂ semi-conducting oxide nano-particles synthesized by polymerizing-complexing sol-gel method. *Physica B Condens. Matter.*, 403:2431, 2008.
- [37] X. Q. Pan and L. Fu. Oxidation and phase transitions of epitaxial tin oxide thin films on (1012) sapphire. *J. Appl. Phys.*, 89(11):6048–6055, 2001.

- [38] J. Geurts, S. Rau, W. Richter, and F. J. Schmitte. SnO films and their oxidation to SnO₂: Raman scattering, IR reflectivity and X-ray diffraction studies. *Thin Solid Films*, 121:217, 1984.
- [39] A. Nikiforov, V. Timofeev, V. Mashanov, I. Azarov, I. Loshkarev, V. Volodin, D. Gulyaev, I. Chetyrin, and I. Korolkov. Formation of SnO and SnO₂ phases during the annealing of SnO(x) films obtained by molecular beam epitaxy. *Appl. Surf. Sci.*, 512:145735, 2020.
- [40] T. G. Novak, P. A. DeSario, J. W. Long, and D. R. Rolison. Designing oxide aerogels with enhanced sorptive and degradative activity for acute chemical threats. *Front. Mater.*, 8:674798, 2021.
- [41] E. G. Lavut, B. I. Timofeyev, V. M. Yuldasheva, E. A. Lavut, and G. L. Galchenko. Enthalpies of formation of tin (iv) and tin (ii) oxides from combustion calorimetry. *The Journal of Chemical Thermodynamics*, 13:635–646, 1981.
- [42] S. Wittmann, M. M. Murshed, and T. M. Gesing. On red tin (II) oxide: temperature-dependent structural, spectroscopic, and thermogravimetric properties. *Z. Anorg. Allg. Chem.*, 648:e202200311, 2022.
- [43] S. M. Ali, J. Muhammad, S. T. Hussain, S. D. Ali, N. U. Rehman, and M. H. Aziz. Annealing effect on structural, optical and electrical properties of pure and Mg doped tin oxide thin films. *J. Mater. Sci. Mater. Electron.*, 24:4925, 2013.
- [44] T. Kaufman-Osborn, E. A. Chagarov, and A. C. Kummel. Atomic imaging and modeling of H₂O₂(g) surface passivation, functionalization, and atomic layer deposition nucleation on the Ge(100) surface. *J. Chem. Phys.*, 140:204708, 2014.